Cancer Cell Internalization of Gold Nanostars Impacts Their Photothermal Efficiency In Vitro and In Vivo: Toward a Plasmonic Thermal Fingerprint in Tumoral Environment

*Ana Espinosa, Amanda K. A. Silva, Ana Sánchez-Iglesias, Marek Grzelczak, Christine Péchoux, Karine Desboeufs, Luis M. Liz-Marzán, and Claire Wilhelm**

Gold nanoparticles are prime candidates for cancer thermotherapy. However, while the ultimate target for nanoparticle-mediated photothermal therapy is the cancer cell, heating performance has not previously been evaluated in the tumoral environment. A systematic investigation of gold nanostar heat-generating efficiency in situ is presented: not only in cancer cells in vitro but also after intratumoral injection in vivo. It is demonstrated that (i) in aqueous dispersion, heat generation is governed by particle size and exciting laser wavelength; (ii) in cancer cells in vitro, heat generation is still very efficient, but irrespective of both particle size and laser wavelength; and (iii) heat generation by nanostars injected into tumors in vivo evolves with time, as the nanostars are trafficked from the extracellular matrix into endosomes. The plasmonic heating response thus serves as a signature of nanoparticle internalization in cells, bringing the ultimate goal of nanoparticle-mediated photothermal therapy a step closer.

1. Introduction

When malignant tumors are deeply embedded within the body or entangled around vital organs, making them inoperable, non-invasive thermal therapy promises to yield better patient outcomes and fewer adverse effects than conventional treatments.[1] Thermal therapy can inflict direct, irreversible cancer cell damage by disrupting their membranes[2] or by denaturing proteins and DNA.[3] Thermal therapy can also be used to enhance cancer cell sensitivity to radiation and chemotherapy.[4] A variety of heat sources have been investigated, including lasers,[5] microwaves,[6] and focused ultrasound,[7] but these approaches also damage healthy tissues situated between the source and the target.[8] In contrast, energy-absorbing nanoparticles can be used to induce heating restricted to the target tissue.[9] Nanoparticle-based thermal therapy is divided into two main categories: magnetothermal and photothermal therapy. Magnetothermal therapy, also called magnetic hyperthermia, is based on the use of a high-frequency alternating magnetic field to excite magnetic nanoparticles and thereby generate local heating.[10] Decades of research have moved the concept of magnetothermal therapy forward from in vitro mechanistic studies[11,12] to preclinical investigations.[13,14] Photothermal therapy is a more recent concept in which light is converted to heat by plasmonic nanoparticles,[15] semiconductor nanocrystals,[16] or carbon-based nanosystems.[17] In recent works, magnetic hyperthermia could be combined with photothermia to amplify heat generation.[18,19] The use of laser sources at 650–950 nm (first near infrared (NIR) window) and 1000–1350 nm (second NIR window) ensures minimal light absorption by surrounding tissues.[20] Efforts to improve light-to-heat conversion efficiency have focused on the size, shape, or surface coating of plasmonic nanoparticles, as well as surface plasmon resonances in the NIR.[21] Gold nanostars are promising candidates, as their plasmon resonance spectra and

Dr. A. Espinosa, Dr. A. K. A. Silva, Dr. C. Wilhelm
Laboratoire Matière et Systèmes Complexes (MSC)
UMR 7057
CNRS and Université Paris Diderot
75205 Paris cedex 13, France
E-mail: claire.wilhelm@univ-paris-diderot.fr
Dr. A. Sánchez-Iglesias, Dr. M. Grzelczak,
Prof. L. M. Liz-Marzán
BioNanoPlasmonics Laboratory
CIC biomaGUNE
Paseo de Miramón 182, 20009 Donostia, San Sebastián, Spain
Dr. M. Grzelczak, Prof. L. M. Liz-Marzán
Ikerbasque, Basque Foundation for Science
48013 Bilbao, Spain
Dr. C. Péchoux
GABI, INRA – MIMA2-MET
AgroParisTech, Université Paris-Saclay
78350 Jouy-en-Josas, France
Dr. K. Desboeufs
LISA, CNRS UMR 7583
Université Paris-Diderot et Université Paris-Est Créteil, 61
av du Général de Gaulles
94010 Créteil, France
Prof. L. M. Liz-Marzán
Biomedical Research Networking Center in Bioengineering
Biomaterials and Nanomedicine (CIBER-BBN)
50018 Aragon, Spain

DOI: 10.1002/adhm.201501035

light absorption efficiency can be precisely tuned by adjusting their width, length, or number of spikes.[22,23]

Despite advances in nanoparticle design, the factors determining light-to-heat conversion efficiency in the tumor environment, which is the ultimate destination of nanoparticles for accomplishing therapy, remain to be fully elucidated. Indeed, most heating studies have used aqueous nanoparticle dispersion, which fail to take into account the effect of the biological environment. For example, magnetic nanoparticles are known to behave differently following protein corona formation or confinement into cellular compartments such as endosomes and lysosomes.[11,24,25] Indeed, magnetic nanoparticles undergo the formation of aggregates in the biological environment, which leads to a divergence in heating efficiency when comparing nanoparticle characterization in aqueous dispersion and real performance in cells.

Decades of intense studies have shown that the efficiency of light energy conversion into heat using plasmonic particles increases with decreasing interparticle distances, i.e., when the particles are in an aggregated state. To enhance such properties in a biological system, nanoparticles can be pre-aggregated, thus controlling beforehand the optical properties and addressing them into the desired system. As an example, Niu and co-workers[26] developed plasmonic vesicles with strong plasmonic coupling that served not only for in vivo imaging but also for remote drug delivery. Nevertheless, such an approach of "pre-aggregation" is synthetically challenging and requires complex surface chemistry. We propose a different strategy, in which living cells (in vivo) take up the initially stable nanoparticles and aggregate them in situ, inducing plasmon coupling and therefore changing their efficiency toward hyperthermia treatment. We thus investigated the light-to-heat conversion efficiency of gold nanostars in environments of increasing complexity, from aqueous dispersion to cancer cells in vitro and then to solid tumors in vivo. This series of heating measurements revealed a thermal fingerprint of plasmonic nanostar internalization by cancer cells.

2. Heating Efficiency of Gold Nanostars in Aqueous Dispersion is Size and Laser-Dependent

We synthesized a panel of five different Au nanostars with sizes ranging from 25 to 150 nm (**Figure 1**A). Transmission electron microscopy (TEM) shows that the nanoparticles comprise a central core from which multiple sharp tips protrude, with narrow size distributions: 27.1 ± 2.2 nm (25-nm sample), 52.6 ± 3.4 nm (55-nm sample), 85.9 ± 4.5 nm (85-nm sample), 121.6 ± 2.9 nm (120-nm sample), and 150.9 ± 2.4 nm (150-nm sample). Size distributions are displayed in Figure S1, Supporting Information. Z-potential and dynamic light scattering (DLS) of the different Au nanostars are shown in Table S1, Supporting Information. As expected, the five samples display distinct UV–vis–NIR optical spectra, all of them featuring a broad plasmon band (Figure 1B). The 25-nm sample yielded two absorbance maxima at around 550 nm and 700 nm, which were attributed to plasmon modes localized at the core and the tips, respectively.[27,28] As the nanostar diameter increased, together with the number of spikes, the influence of the core on the extinction spectrum gradually declines,[28] eventually resulting in a single band. Regarding 55-nm, 85-nm, 120-nm, and 150-nm nanostars, the single absorbance band gradually shifts toward the NIR region, at 790, 800, 900, and 950 nm, respectively, confirming that nanostar plasmon resonances are strongly dependent on size and morphology, especially spike length and number of spikes.[23,29,30]

The photothermal heating efficiency of the nanostar samples, dispersed in water at the same Au concentration of 0.75×10^{-3} M, was monitored with an infrared (IR) thermal camera (images are shown in Figure 1C and Figure S2, Supporting Information) during laser irradiation at 680, 808, and 1064 nm, at the same power setting of 1 W cm^{-2}. The temperature was observed to rise as a function of time at all wavelengths and with all five samples, reaching saturation after 5–10 min (see typical temperature curves in Figure 1D and Figure S3, Supporting Information). The average values of temperature increment recorded after 1 min, $\Delta T_{1\text{min}}$, as well as the temperature increase reached at saturation $\Delta T_{\text{plateau}}$ are plotted in Figure 1E,F, respectively. A remarkable correlation between the light-to-heat conversion profiles and the UV–vis–NIR absorption spectra was observed (see Figure S4, Supporting Information, for quantitative comparison). For instance, the 25-nm nanostars displayed the best heating efficiency ($\Delta T_{1\text{ min}}$ = 19 °C; $\Delta T_{\text{plateau}}$ = 44 °C) when irradiated at 680 nm, close to the maximum of the localized surface plasmon resonance (LSPR) band. Conversely, the weakest heating effect ($\Delta T_{1\text{ min}}$ = 3 °C; $\Delta T_{\text{plateau}}$ = 6 °C) was observed at the wavelength at which spectral absorbance was lowest (1064 nm). Similar results were obtained with the 85-nm nanostar sample, for which the maximum of the LSPR band was near 808 nm. This sample showed average temperature increments of ($\Delta T_{1\text{ min}}$ = 13 °C; $\Delta T_{\text{plateau}}$ = 33 °C), ($\Delta T_{1\text{ min}}$ = 18 °C; $\Delta T_{\text{plateau}}$ = 42 °C), and ($\Delta T_{1\text{ min}}$ = 5 °C; $\Delta T_{\text{plateau}}$ = 10 °C) at laser wavelengths of 680, 808, and 1064 nm, respectively. With the 150-nm nanostar sample, because the laser wavelength settings corresponded to neither the maximum nor the minimum absorption, ΔT values were similar at all three wavelengths (($\Delta T_{1\text{ min}}$ = 10 °C; $\Delta T_{\text{plateau}}$ = 28 °C), ($\Delta T_{1\text{ min}}$ = 13 °C; $\Delta T_{\text{plateau}}$ = 30 °C), ($\Delta T_{1\text{ min}}$ = 16 °C; $\Delta T_{\text{plateau}}$ = 29 °C) for 680, 808, and 1064 nm, respectively).

As shown in Figure 1E,F, for a given laser wavelength (dotted lines on the graphs), the heating efficiencies were red-shifted as the nanostar size increased. At 680 nm, the 25-nm sample was most efficient, whereas the 150-nm sample dominated at 1064 nm. The intermediate sizes (55, 85, and 120 nm) were similarly efficient at 808 nm, and all three were more efficient than the 25 and 150 nm samples. Thus, precise nanostar design features result in distinct and well-defined photothermal conversion profiles, which is consistent with their absorption spectral features.

Importantly, excellent absolute heating efficiency was obtained at the appropriate laser settings. To eliminate the influence of the experimental conditions (sample concentration, geometry determining the saturation temperature), this heating efficiency is expressed with a parameter called the specific absorption rate (SAR, expressed in W g^{-1} of Au, see the Supporting Information), which is calculated from the initial slope of the temperature curves as a function of time (values are presented in Figure 1E). Under optimal conditions, all five samples reached a SAR of nearly 10 kW g^{-1} at a laser power of 1 W cm^{-2}. This is one of the highest SAR values reported at this laser power. Higher values, such as 430 ± 40 and 190 ± 20 kW g^{-1} (at 800 nm), have been

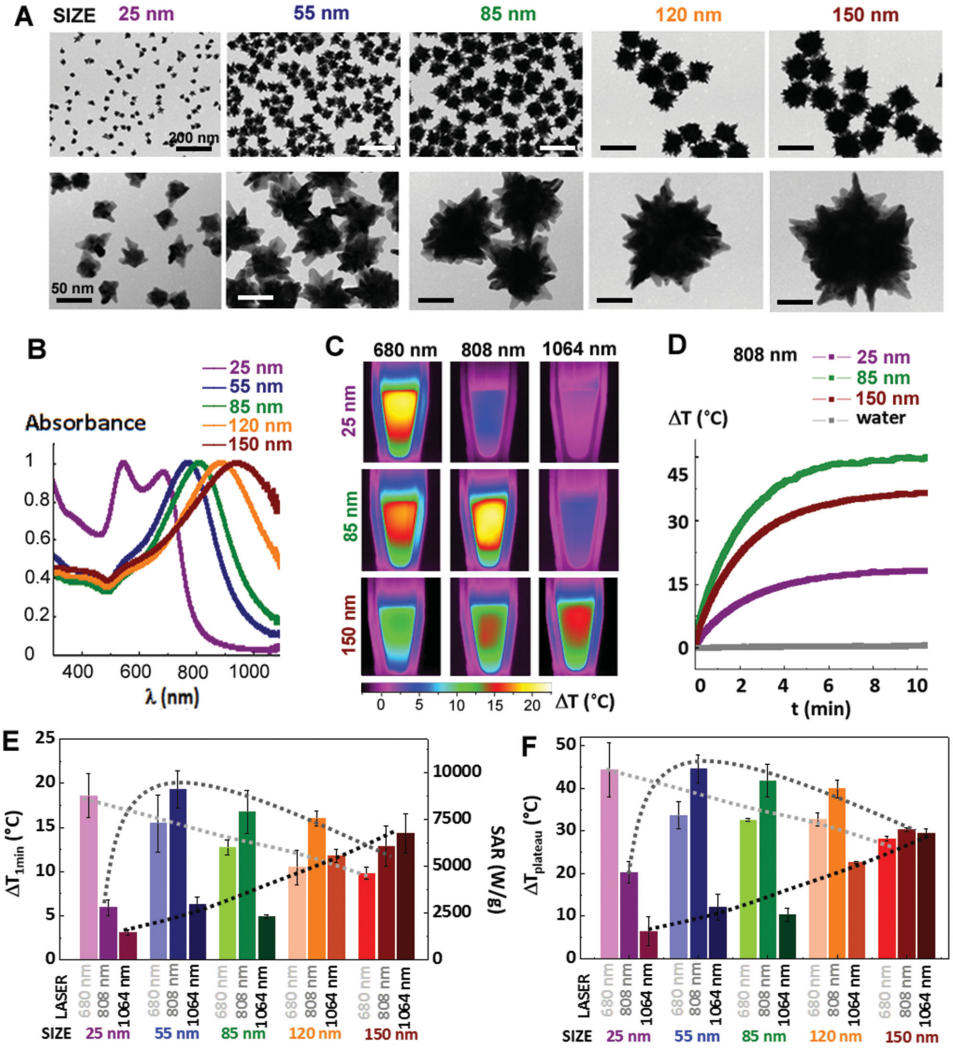

Figure 1. Gold nanostars in aqueous dispersion: influence of nanostar size and laser excitation wavelength on plasmonic resonances and heating efficiency. A) Representative TEM images of the five samples of Au nanostars, at low (top, scale bar = 200 nm) and high (bottom, scale bar = 50 nm) magnification. B) UV–vis–NIR absorption spectra of the same samples: the LSPR band shifts from 600 to 1000 nm as the nanostar size increases. C) Infrared thermal images of aqueous dispersions (150 µL) of Au nanostars (25, 85, and 150 nm samples) at [Au] = 0.75×10^{-3} M, after 1 min of laser irradiation at 680, 808, and 1064 nm and 1 W cm^{-2}. D) Temperature increase curves for the 25, 85, and 150 nm samples upon irradiation at 808 nm (1 W cm^{-2}). E,F) Temperature increments achieved with all five samples (25, 55, 85, 120, and 150 nm) as a function of laser wavelength (680, 808, and 1064 nm), after E) 1 min ($\Delta T_{1\ min}$) or F) 10 min (plateau, $\Delta T_{plateau}$) of exposure at 1 W cm^{-2}.

reported with gold nanorods and nanostars, respectively, but at much stronger laser powers (13 W cm^{-2}).[2,31]

As cancer cells are the main target of nanostar-based photothermal therapy, we next investigated Au nanostar heating efficiency in vitro (nanostars internalized by cancer cells), and in vivo (after intratumoral injection).

3. Interaction of Au Nanostars with Cancer Cells: Internalization and Heating Efficiency

The photothermal conversion efficiency of the three most representative nanostar samples covering the whole size range were selected (25, 85, and 150 nm) and first monitored in vitro, using the human prostate cancer cell line PC3. Nanostar uptake was investigated by TEM using fixed samples and Au elemental analysis (see the Supporting Information). **Figure 2**A (and Figure S5, Supporting Information) shows cells incubated with nanostars in complete culture medium Dulbecco's modified Eagle's medium (DMEM supplemented with 10% fetal bovine serum (FBS)) overnight (16 h) at [Au] = 0.02×10^{-3} M. The nanostars, visualized as electron-dense spots, were all located within endosomes, close to one another. No nanostars were found in the extracellular medium or attached to the cell outer membrane. These observations are in agreement with those of previous studies where accumulation of Au nanostars was observed by TEM within endosomes.[32,33]

Elemental analysis (inductively coupled plasma atomic emission spectroscopy (ICP-AES)) confirmed such an efficient cellular uptake, which increased with nanostar size from

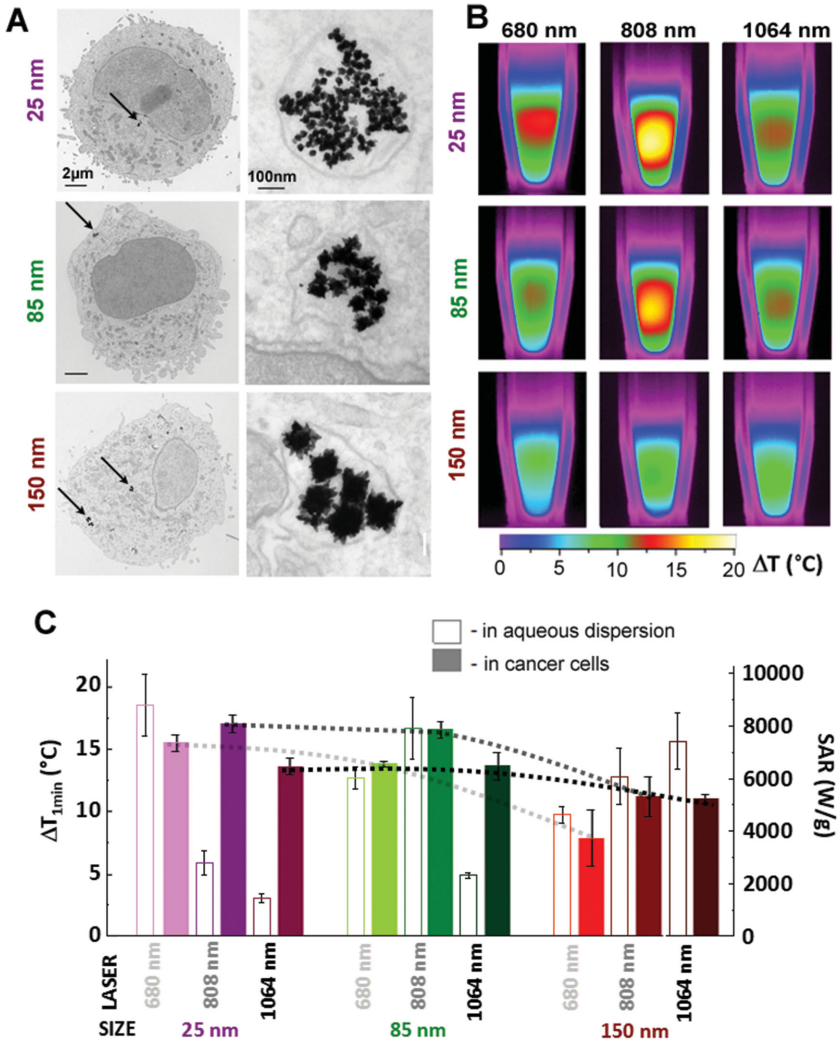

Figure 2. Interaction of Au nanostars with cancer cells, and intracellular heating efficiency. A) TEM images of PC3 cancer cells after incubation with Au nanostars, at different magnifications (scale bars 2 μm and 100 nm). B) Typical infrared thermal images of the cell samples (about 15 million cells containing Au nanostars dispersed in 150 μL of PBS, adjusted to a concentration of [Au] = 0.75×10^{-3} M). From top to bottom, cells incubated with 25, 85, and 150 nm nanostars after 1 min of laser irradiation at 680, 808, and 1064 nm and 1 W cm^{-2}. C) Average temperature increase for all cell samples as a function of laser wavelength (680, 808, and 1064 nm) after 1 min at 1 W cm^{-2}. On the same graph the calculated values for nanostars in aqueous dispersion are shown (empty bars). SAR (in kW g^{-1}, secondary right axis) was also calculated (see Experimental Details in the Supporting Information) for all cellular samples.

1.4 ± 0.1 pg Au/cell for the 25-nm sample to 2.6 ± 0.3 and 3.0 ± 0.3 pg Au/cell for the 85 and 150 nm samples, respectively (graph shown in Figure S6A, Supporting Information). Uptake was within the same range, whatever the nanostar size. Besides, as shown also in Figure S6B, Supporting Information, nanostar internalization did not affect cell metabolic activity, regardless of the particle size, in agreement with previous reports.[30,33,34] It then clearly appeared that nanostar heating efficiency was modified following cellular internalization. Nanostar-loaded cells were harvested in a pellet. The number of cells per mL was then determined (through cell counting in a Malassez chamber) to finally obtain the Au mass per mL (Au concentration of the pellet). They were resuspended in a volume of 150 μL to match the Au concentration of 0.75×10^{-3} M, the same as used for the aqueous nanostar dispersion. The heating was recorded with IR camera and the same set-up as the one used for the aqueous dispersions (Figure 2B,C shows typical IR images and average temperature increase, respectively, after 1 min laser exposure). At the highest laser wavelength (1064 nm), the 1 min temperature increment ΔT_{1min} rose from 3 up to 13 °C with the 25-nm nanostars and from 5 up to 13 °C with the 85-nm nanostars, while it dropped from 16 down to 11 °C with the 150-nm nanostars. With the 25-nm nanostars, ΔT_{1min} was still higher at 680 nm than at 1064 nm (15 vs. 13 °C), but its highest value was found at 808 nm (17 °C). At a wavelength of 680 nm, the decline in heating efficiency with size observed in aqueous dispersion (nanostar size is represented by dotted lines in Figure 2C) was much less marked when the nanostars were confined within cells (data in aqueous dispersion are shown as empty bars in Figure 2C for a direct comparison). Similarly, the maximum heating observed at 808 nm with the intermediate-size nanostars in aqueous dispersion was not observed, and neither was the size-dependent increase in heating efficiency at 1064 nm.

We thus conclude that the wavelength dependence of nanostar heating efficiency was reduced upon confinement in endosomal compartments. Indeed, while the laser wavelength markedly influenced heating efficiency in aqueous dispersion (respective 95% and 80% decreases in heating efficiency with the 25-nm and 85-nm nanostars irradiated with the "correct" and "incorrect" wavelengths), this was far less the case in the cellular environment (–20% and –17%, respectively). Finally, the heating power (SAR) (also shown in Figure 2C) of the different nanostar-loaded cell samples followed the same trend: the SAR inside cancer cells was much less dependent on nanostar size but still reached high values, in the range of 10 kW g^{-1}.

The most likely explanation for this attenuation of wavelength dependence upon cellular uptake is nanostar confinement within endosomes. Indeed, Au nanoparticle aggregation in endosomes was recently measured and led to LSPR red-shift and broadening.[35] Similarly, using plasmonically enhanced Rayleigh imaging of living cells, the subcellular aggregation of Au nanoparticles in endosomes was demonstrated through the red-shift and broadening of the plasmon band.[36] The macroscopic UV–vis–NIR spectra of Au nanostars in cells are shown in Figure S7, Supporting Information. While acquisition was hindered by cellular background structures, these spectra reveal a flattening of the extinction bands, a decline in the peak-to-valley distance, and a red-shift.

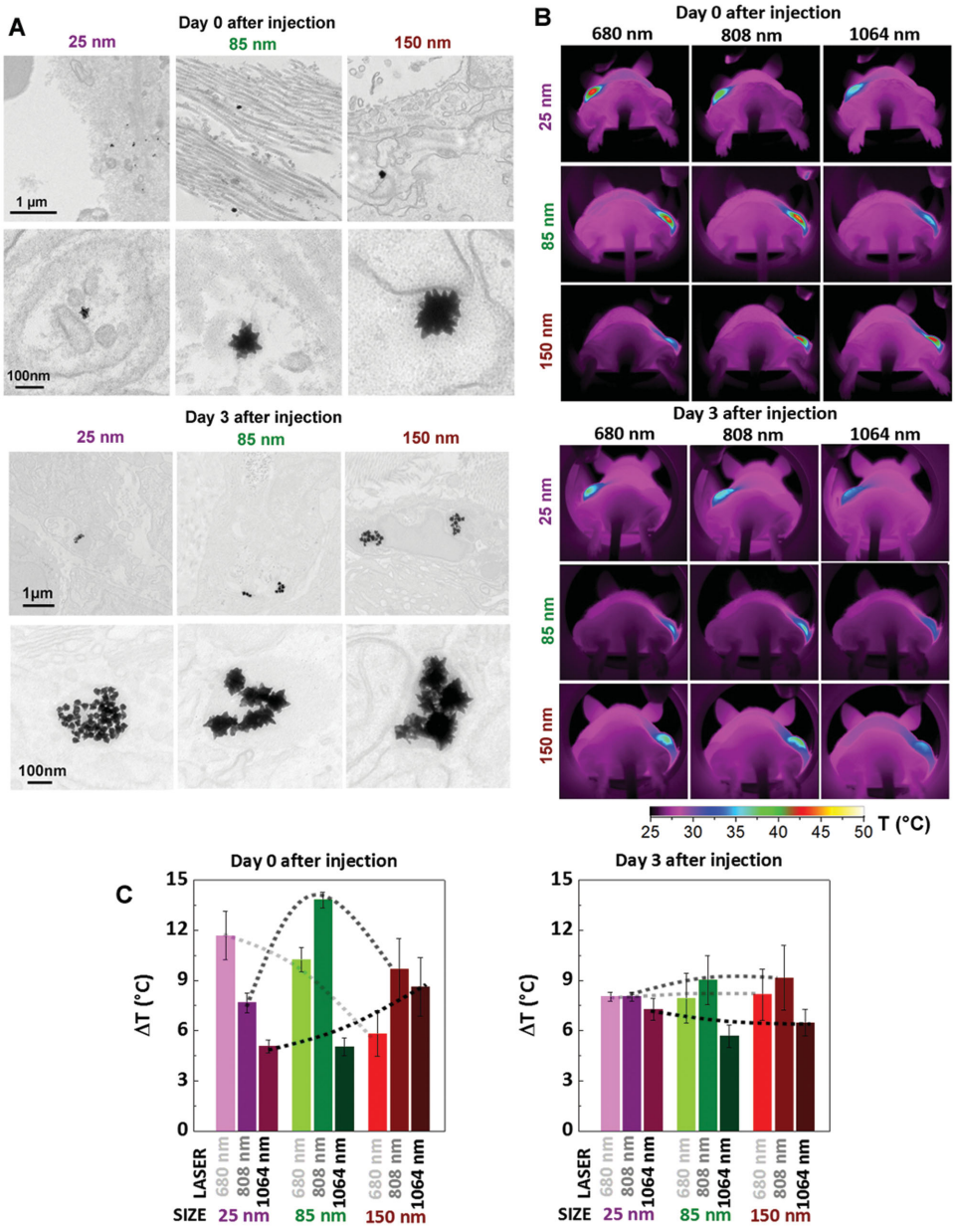

Figure 3. Heating efficiency of Au nanostars in tumors in vivo: evolution over time. A) TEM images of nanostars on day 0 and day 3 after intratumoral injection. B) In vivo infrared thermal images of tumors injected with 25, 85, and 150 nm nanostars and exposed for 1 min to 680, 808, and 1064 nm laser irradiation at 1 W cm^{-2}, on day 0 (1 h after injection, upper panel) and on day 3 (lower panel). C) Average tumoral temperature increase as a function of the laser wavelength (680, 808, and 1064 nm) and nanostar size, after 1 min of exposure at 1 W cm^{-2}, on day 0 (left) and day 3 (right). Dotted lines serve to visualize the evolution of heat generation according to nanostar size, for a given laser wavelength (light gray for 680 nm, gray for 808 nm, and dark gray for 1064 nm).

4. Heating Efficiency of Au Nanostars In Vivo: Evolution Post-injection

Heating efficiency in vivo was evaluated by injecting nanostars (at the same [Au] = 0.75×10^{-3} M) into PC3 tumors induced in mice. The uptake and heating efficiency of 25, 85, and 150 nm nanostars were investigated on days 0 and 3 post-injection. Intratumoral nanostar localization was assessed by TEM, and local tumoral temperature changes were monitored in living mice with the infrared thermal camera during the entire period of irradiation.

On day 0, TEM images (**Figure 3**A, top) showed individual nanostars dispersed close to vessels, throughout the extracellular medium, or within bundles of collagen fibres (see also Figures S8–S10, Supporting Information). Of note, no nanostars were observed in the cytoplasm. On day 3, the nanostars were located solely in endosomes (Figure 3A, bottom and Figures S11–S14, Supporting Information), inside tumor

cells, forming small random clusters, but retaining the original branched morphology, i.e., no reshaping has taken place within the tumor. This is an important point considering that nanostar reshaping may further influence nanoparticle LSPR.[37] Thus, as previously observed in cancer cells in vitro, all Au nanostars were processed into subcellular compartments in vivo where they accumulate.

Figure 3B shows thermal images after 1 min of tumor irradiation on day 0 (1 h after injection) and on day 3, while Figure 3C shows the average temperature increment ΔT_{1min}. On day 0, the photothermal conversion profile was similar to that of dispersed nanostars (Figure 3C, left). Note that the nanostar dispersion (50–100 µL) at [Au] = 0.75×10^{-3} M was injected into tumors. The volume injected depended on the tumor volume; For each tumor, the nanostars injected volume was adjusted in order to keep the dilution factor constant. It clearly appears from the thermal images that heating remains localized close to the site of injection. In keeping with this observation, the values of temperature increase were found to be in the same range as those obtained in dispersion or in cancer cells (at [Au] = 0.75×10^{-3} M). For instance, with 25-nm nanostars, the tumor temperature rose (at day 0, right after injection) by respectively 12, 8, and 5 °C after 1 min of irradiation (1 W cm^{-2}) at 680, 808, and 1064 nm. In the same conditions, the respective temperature increments were about 10, 14, and 5 °C with 85-nm nanostars and about 6, 10, and 9 °C with 150-nm nanostars. Untreated tumors exposed to laser irradiation showed a negligible temperature rise of 3–4 °C (Figure S15, Supporting Information). The in vivo light-to-heat conversion profile evolved with time, markedly differing between day 0 and day 3 with both 25-nm and 85-nm nanostars (Figure 3C, right). Remarkably, the photothermal efficiency on day 3 showed the same pattern as that of nanostars internalized by cancer cells in vitro. This is in perfect agreement with TEM observations, which showed that all nanostars were confined in endosomes. On day 3 the recorded temperature increments were thus independent of nanostar size and laser wavelength.

5. In Vivo Thermal Signature of Intratumor Localization of Plasmonic Nanoparticles

Here, we demonstrate that the heating efficiency at different laser wavelengths remarkably matches the degree of plasmonic gold nanostars internalization by cancer cells in vivo. We therefore provide information on the nanoscale cellular fate of plasmonic nanoparticles within a tumor, through simple measurement of heat generation upon irradiation at different wavelengths, by contrast with the initial wavelength-dependent heating profile in aqueous dispersion.

The relationship between macroscopic physical measurements (magnetic, optical, thermal, etc.) and the nanoscale localization of nanomaterials in living environments has rarely been studied. Recently, Di Corato et al.[11] and Soukup et al.[24] showed that magnetic heat generation (magnetic hyperthermia) can reveal the local organization of magnetic nanoparticles, providing a magnetic heating signature related directly to the nanoparticles' local anisotropy and interactions. These measurements were performed in situ in cellular samples (in vitro), with magnetic nanoparticles confined within endosomes and in very close mutual contact. The strong confinement of the particles and their interactions provoked steric frustration which in turn modified the magnetic dynamics responsible for heat generation, resulting in a drop in heating efficiency after cancer cell uptake.

Here, we demonstrate that intracellular confinement of plasmonic nanoparticles in endosomes also impacts their photothermal efficiency. Whereas magnetic hyperthermia measurements had previously only been made in vitro, we show that this thermal signature also exists in vivo, after cellular internalization within a tumor. To the best of our knowledge, this is the first report on photothermal measurements as a way for real-time probing the effect of the biological microenvironment on the plasmonic properties of nanoparticles in situ. By providing insights into nanoparticles/microenvironment interactions, this approach offers the opportunity to non-invasively assess cellular uptake of nanoparticles. Considering in vivo applications, depicting the interplay of nanoparticles with biological media at each step of their lifetime cycle (from aqueous dispersion to cell internalization) is a critical point for ultimate implementation of nanostar-mediated photothermal therapy settings.

Besides, these results are in agreement with the observation that the plasmon characteristics of individual gold nanoparticles evolve when the particles form clusters,[35] sometimes even producing a synergistic effect. This is what is observed here, at a given laser wavelength, with 25-nm gold nanostars: when irradiated at 808 nm, at the same concentration, these nanostars deliver only a 6 °C temperature increase when individually dispersed in solution, while the temperature increment leaps to almost 20 °C upon aggregation inside cells.

6. Strategy Selection for Photothermal Therapy

This particular case of 25-nm nanostars raises questions as to the best strategy for translating plasmonic photothermia from the laboratory to the clinic. Measurements in aqueous dispersions suggested that 25-nm nanostars would not be suitable for in vivo applications, given their low NIR absorption. Indeed, at 808 nm, larger nanostars (>50 nm) yielded a 200% increase in heat generation. Yet, in vivo, after processing by cancer cells (day 3), 25-nm nanostars were as efficient as 85-nm and even 150-nm nanostars.

Advances in colloid chemistry have enabled the synthesis of nanoparticles with tightly controlled sizes and shapes,[38] allowing fine-tuning of their physical properties. Here we demonstrate that gold nanostar heating efficiency in dispersion can be tuned by adjusting their size or the laser excitation wavelength. Although spectroscopy and thermal measurements have been widely used to characterize and optimize the design of plasmonic nanoparticles in aqueous dispersion, we show here that the recorded photothermal conversion efficiencies are not predictive of the values achieved in either isolated cells or living tissues. Moreover, we show that, regardless of their size, nanostars confined within tumor cell endosomes exhibit similar heating efficiencies upon near-infrared laser excitation. Thus, because their small size should facilitate biodistribution

in vivo, we propose that 25-nm nanostars are the candidates of choice for photothermal tumor therapy.

From a pharmacokinetic standpoint, nanoparticle size is a key property as it determines interactions with cells, the vasculature and interstitial transport. Indeed, the size of nanoparticles directly influences the interaction with the local fenestrated vasculature. Nanoparticle size should be inferior to vasculature fenestration cut-off in order to allow tumor accumulation by the enhanced permeability and retention effect.[39] Considering gold nanoparticles, it has been reported that they should feature sub-100 nm size range to be able to cross tumor vasculature and move throughout the tumor interstitium.[40] In this regard and taking into account the photothermal conversion profile reported herein after processing by cancer cells, the smallest gold nanostars in the 25–50 nm size range should definitely be considered best suited for photothermal cancer therapy.

Concerning the in vivo model, intratumoral injection in subcutaneous mice tumor is a convenient cancer model for assessing nanoscale cellular heating conversion of plasmonic nanoparticles. This model is suitable to track the nanophysical properties of nanomaterials measuring the thermal efficiency feature in a superficial (accessible to laser irradiation) and localized tumor, ensuring high accumulation of nanomaterials. In the case of systemic administration, the injected nanoparticles would probably be uptaken by several organs such as lungs, liver, and spleen and only a fraction of it would reach the tumor site. As a result, we could expect to observe similar heating conversion to the applied laser wavelengths but at a reduced intensity degree, as a function of the amount of nanomaterial that would reach the tumor site. However, it is noteworthy to mention that even if nanoparticles would be distributed throughout the organism, the heating effect would remain confined to tumor site as it is triggered by local laser exposure at the tumor region.

7. Conclusion

In summary, by testing a variety of gold nanostars with average diameters ranging from 25 to 150 nm, and plasmonic resonance peaks between 500 and 1000 nm, we found that heating efficiency in aqueous dispersion depends on both particle size and excitation laser wavelength. However, when the nanostars were internalized by cancer cells and confined in endosomes, size and wavelength dependence are strongly attenuated or even suppressed. Attenuation was also observed in vivo when the nanostars were injected into solid tumors, but only after cellular uptake, which is reflected in the temperature profiles obtained at different laser wavelengths. In view of this measured in vivo behavior, we infer that the most important design feature of gold nanostars for thermotherapy is not their adjusted plasmonic peak measured in aqueous dispersion, but rather their size and coating to ensure optimal biodistribution in vivo.

8. Experimental Section

Gold Nanostar Synthesis—Chemicals: Gold (III) chloride trihydrate ($HAuCl_4$), sodium citrate tribasic dihydrate, polyvinylpyrrolidone (PVP, average M_W = 10 000), *N*,*N*-dimethylformamide (DMF) were purchased from Sigma–Aldrich. Ethanol was purchased from Sharlau. All reactants were used without further purification.

Gold Nanostar Synthesis—Synthesis of Gold Seeds (14 and 40 nm): Two batches of citrate-stabilized gold seeds were prepared. Gold seeds with diameter of 14.3 ± 0.2 nm were prepared according to the method by Enustun and Turkevich.[41] The seeds with diameter of 40.2 ± 1.2 nm were prepared according to method by Puntes and co-workers.[42]

Gold Nanostar Synthesis—Functionalization with PVP: Citrate-stabilized gold seeds (14 and 40 nm) were functionalized with PVP using Graf method.[43] The amount of PVP was calculated to provide ≈60 molecules per nm^2 of particles surface. The PVP was dissolved in water in ultrasonic bath for 15 min. Subsequently, the solution containing PVP was added dropwise to the solution containing citrate-stabilized gold seeds under stirring. To ensure the adsorption of the polymer on particles surface, the reaction mixture was stirred overnight at room temperature. Finally, the PVP-stabilized gold seeds were centrifuged (14 nm–4000 rpm; 40 nm–1200 rpm) and redispersed in ethanol. The final concentration of gold was adjusted to 3×10^{-3} M for both seeds solution.

Gold Nanostar Synthesis—Synthesis Gold Nanostars (25 nm, 55 nm): Gold nanostars were prepared by following the protocol by Kumar et al.[44] Briefly, an aqueous solution of $HAuCl_4$ (0.041 mL, 100×10^{-3} M) was mixed with a solution of PVP (15 mL, 10×10^{-3} M) in DMF. The mixture was stirred until complete disappearance of the Au^{+3} CTTS band at 325 nm, followed by rapid addition of gold seeds (14 nm) in ethanol under vigorous stirring. To obtain nanostars with 25 and 55 nm of diameter, the volume of seeds was found to be 0.292 and 0.023 mL, respectively. The color of the solution changes from colorless to blue within 40 min, indicating the formation of gold nanostars. The samples were centrifuged three times and redispersed in water.

Gold Nanostar Synthesis—Synthesis Gold Nanostars (85 nm, 120 nm, 150 nm): An aqueous solution of $HAuCl_4$ (0.041 mL, 100×10^{-3} M) was mixed with a solution of PVP (15 mL, 10×10^{-3} M) in DMF. The mixture was stirred until complete disappearance of the Au^{+3} CTTS band at 325 nm, followed by rapid addition of gold seeds (40 nm) in ethanol under vigorous stirring. To obtain nanostars with 85, 125, and 150 nm of diameter, the volume of seeds was found to be 0.159, 0.053, and 0.026 mL, respectively. The color of the solution changes from colorless to blue within 40 min, indicating the formation of gold nanostars. The samples were centrifuged three times and redispersed in water.

Dynamic Light Scattering Analysis: DLS curves of the size distribution were obtained using NanoSizer (Zeta-Sizer, Malvern Instrument, UK).

Cell Culture, Labelling and Uptake Assays: Human prostate cancer cells (PC3, ATCC CRL-1435) were cultured in DMEM supplemented with 10% FBS and 1% penicillin, and maintained at 37 °C with 5% CO_2 until confluence.

Cells were incubated with nanostars of different sizes (from 25 to 150 nm) at [Au] = 0.02×10^{-3} M for 16 h in Roswell Park Memorial Institute medium (RPMI) at 37 °C in two 150-cm^2 flasks (≈30 million cells). The medium was then removed and the cells were washed with culture medium. Labelled cells were detached, centrifuged and resuspended in PBS for further experiments.

Elemental Analysis: The concentration of gold in nanostar aqueous dispersion and cells was analyzed by ICP-AES. The samples were digested in concentrated HNO_3 for 1 h at 90–100 °C, then recovered and diluted in 1% HCl.

UV–vis–NIR Spectroscopy: Optical absorption measurements of Au nanostars in aqueous dispersion and in cancer cells in vitro were carried out in commercial spectrophotometers (Agilent 8453 and 50 scan Cary, Varian) in the 300–1100 nm spectral range. Sample preparation (preparation of a cell lysate excluding the nuclei) for acquiring the cellular spectra is described in the caption of Figure S7, Supporting Information.

Cytotoxicity Assay: Cell viability after incubation with the different Au nanostars was evaluated in the Alamar Blue assay (Life Technologies). Labelled cells were incubated with 10% Alamar Blue in DMEM without red phenol for 2 h and then transferred to a 96-well plate for analysis with a microplate reader (BMG FluoStar Galaxy) at an excitation wavelength of 550 nm with fluorescence detection at 590 nm. Viability

was determined by comparison with control cells (100%). All reported experiments were performed in triplicate.

Photothermal Measurements in Aqueous Dispersion and in Cells In Vitro: Photothermal measurements were made with visible and NIR lasers (680, 808, and 1064 nm; Laser Components S.A.S (France)) with external adjustable power settings (0–5 W). The sample (aqueous nanoparticle dispersion or suspension of Au nanostar-loaded cells) contained in a 0.5-mL tube was illuminated at 2.5–3 cm distance with a laser spot of 1 cm^2. The laser power was fixed at 1 W cm^{-2}. The temperature elevation was recorded with an infrared thermal imaging camera (FLIR SC7000) in real time, every second, in the temperature range of 25 to 70 °C. The temperature elevation was measured as a function of time (dT/dt) at the initial linear slope ($t \approx 30$ s) in order to evaluate the heating effect in terms of SAR, power dissipation per unit mass of element (W g^{-1}). SAR was calculated using the following formula:

$$SAR = \frac{CV_s}{m}\frac{dT}{dt}$$

where m is the total mass of gold in the sample, C is the specific heat capacity of the sample (C_{water} = 4185 J L^{-1} K^{-1}, C_{cell} = 4125 J L^{-1} K^{-1}), and V_s is the sample volume.

Photothermal Measurements In Vivo: Six-week-old Naval Medical Research Institute (NMRI) male nude mice weighing 20 ± 1 g, provided by Janvier Laboratories France, were hosted in the facilities of Animalerie Buffon, Institute Jacques Monod, Paris 7 University. They were acclimatized for 1 week before use, in keeping with European standards of animal care and well-being.

Solid tumors were induced by subcutaneous injection of 2×10^6 PC3 human prostate carcinoma cells in 100 µL of physiological saline (PBS) in the left and right flanks. When the tumors reached a volume of about 125 mm^3, they were injected with 100 µL of Au nanostars (25, 85, or 150 nm) in saline dispersion at [Au] = 0.75×10^{-3} M. Twenty-one tumors in 12 animals were divided into four groups: 6 tumors were injected with 25-nm Au nanostars, 6 with 85-nm Au nanostars, and 6 with 150-nm Au nanostars; 3 noninjected tumors served as controls. The tumors were illuminated with three lasers (680, 808, and 1064 nm) at 1 W cm^{-2} at a distance of 3 cm for 5 min on days 0, 1, and 3 postinjection. The tumor surface temperature was monitored with an infrared thermal camera (FLIR SC7000, FLIR Systems, Inc.), each measurement being made in triplicate. During the measurements the animals were anesthetized with ketamine/xylazine. The animals were sacrificed when collateral tumors reached 1 cm^3.

TEM: TEM images of aqueous dispersion were obtained with a JEOL JEM-1400PLUS transmission electron microscope operating at an acceleration of 120 kV (CIC biomaGUNE, Spain).

TEM micrographs of Au nanostars in cells were acquired using a Hitachi HT7700 operating at 80 kV (MIMA2 platform, INRA, Jouy-en-Josas, France). Tumor cells were incubated with Au nanostars and fixed with 5% glutaraldehyde in 0.1 mol L^{-1} sodium cacodylate buffer, then gradually dehydrated in ethanol and stained with 1% osmium tetroxide and 1.5% potassium cyanoferrate. The samples were embedded in Epon and sectioned for analysis. Mouse tumors were cut into 1 mm^3 pieces, fixed with 2% glutaraldehyde in 0.1 M sodium cacodylate buffer and kept in 0.1 M sodium cacodylate and 0.2 M sucrose buffer, then postfixed with the same protocol as for isolated tumor cells before being cut into thin sections (70 nm) for observation.

Supporting Information

Supporting Information is available from the Wiley Online Library or from the author.

Acknowledgements

This work was supported by the Marie Curie Intra-European Project FP7-PEOPLE-2013-740 IEF-62647. The authors are grateful to A. Djemat from Animalerie Buffon for animal care. L.M. L.-M. acknowledges funding from the European Research Council (ERC Advanced Grant #267867, Plasmaquo) and the Spanish Ministerio de Economía y Competitividad (MAT2013-46101-R).

Received: December 21, 2015
Revised: January 22, 2016
Published online: March 15, 2016

[1] a) P. Moroz, S. K. Jones, B. N. Gray, *J. Surg. Oncol* **2001**, *77*, 259; b) M. Ahmed, S. N. Goldberg, *J. Vasc. Interv. Radiol.* **2002**, *13*, S231.
[2] J. C. Bischof, J. Padanilam, W. H. Holmes, R. M. Ezzell, R. C. Lee, R. G. Tompkins, M. L. Yarmush, M. Toner, *Biophys. J.* **1995**, *68*, 2608.
[3] a) J. R. Lepock, K.-H. Cheng, H. Al-qysi, I. Sim, C. J. Koch, J. Kruuv, *Int. J. Hyperthermia* **1987**, *3*, 123; b) J. R. Lepock, H. E. Frey, A. M. Rodahl, J. Kruuv, *J. Cell. Physiol.* **1988**, *137*, 14.
[4] a) P. Wust, B. Hildebrandt, G. Sreenivasa, B. Rau, J. Gellermann, H. Riess, R. Felix, P. M. Schlag, *The Lancet Oncol.* **2002**, *3*, 487; b) R. W. Habash, R. Bansal, D. Krewski, H. T. Alhafid, *Crit. Rev. Biomed. Eng.* **2006**, *34*, 459.
[5] M. Castrén-Persons, T. Schröder, O. Rämö, P. Puolakkainen, E. Lehtonen, *Lasers Surg. Med.* **1991**, *11*, 595.
[6] T. Seki, M. Wakabayashi, T. Nakagawa, M. Imamura, T. Tamai, A. Nishimura, N. Yamashiki, A. Okamura, K. Inoue, *Cancer* **1999**, *85*, 1694.
[7] F. A. Jolesz, K. Hynynen, *Cancer J.* **2001**, *8*, S100.
[8] E. S. Day, J. G. Morton, J. L. West, *J. Biomech. Eng.* **2009**, *131*, 074001.
[9] D. Jaque, L. M. Maestro, B. Del Rosal, P. Haro-Gonzalez, A. Benayas, J. Plaza, E. M. Rodríguez, J. G. Solé, *Nanoscale* **2014**, *6*, 9494.
[10] a) G. Vallejo-Fernandez, O. Whear, A. Roca, S. Hussain, J. Timmis, V. Patel, K. O'Grady, *J. Phys. D: Appl. Phys.* **2013**, *46*, 312001; b) R. E. Rosensweig, *J. Magn. Magn. Mater.* **2002**, *252*, 370.
[11] R. Di Corato, A. Espinosa, L. Lartigue, M. Tharaud, S. Chat, T. Pellegrino, C. Ménager, F. Gazeau, C. Wilhelm, *Biomaterials* **2014**, *35*, 6400.
[12] a) V. Connord, P. Clerc, N. Hallali, D. El Hajj Diab, D. Fourmy, V. Gigoux, J. Carrey, *Small* **2015**, *11*, 2437; b) I. Andreu, E. Natividad, L. Solozábal, O. Roubeau, *ACS Nano* **2015**, *9*, 1408.
[13] a) K. Maier-Hauff, F. Ulrich, D. Nestler, H. Niehoff, P. Wust, B. Thiesen, H. Orawa, V. Budach, A. Jordan, *J. Neurooncol.* **2011**, *103*, 317; b) K. Maier-Hauff, R. Rothe, R. Scholz, U. Gneveckow, P. Wust, B. Thiesen, A. Feussner, A. von Deimling, N. Waldoefner, R. Felix, *J. Neurooncol.* **2007**, *81*, 53.
[14] R. Di Corato, G. Béalle, J. Kolosnjaj-Tabi, A. Espinosa, O. Clément, A.K.A. Silva, C. Ménager, C. Wilhelm, *ACS Nano* **2015**, *9*, 2904.
[15] S. Lal, S. E. Clare, N. J. Halas, *Acc. Chem. Res.* **2008**, *41*, 1842.
[16] T. N. Lambert, N. L. Andrews, H. Gerung, T. J. Boyle, J. M. Oliver, B. S. Wilson, S. M. Han, *Small* **2007**, *3*, 691.
[17] G. Lamanna, A. Battigelli, C. Ménard-Moyon, A. Bianco, *Nanotechnol. Rev.* **2012**, *1*, 17.
[18] A. Espinosa, M. Bugnet, G. Radtke, S. Neveu, G.A. Botton, C. Wilhelm C, A. Abou-Hassan, *Nanoscale* **2015**, *7*, 18872.
[19] A. Espinosa, R. Di Corato, J. Kolosnjaj-Tabi, P. Flaud, T. Pellegrino, C. Wilhelm, *ACS Nano* **2016**, *10*, 2436.
[20] a) B. Chance, *Ann. N. Y. Acad. Sci.* **1998**, *838*, 29; b) M.-F. Tsai, S.-H. G. Chang, F.-Y. Cheng, V. Shanmugam, Y.-S. Cheng, C.-H. Su, C.-S. Yeh, *ACS Nano* **2013**, *7*, 5330.
[21] E. C. Dreaden, A. M. Alkilany, X. Huang, C. J. Murphy, M. A. El-Sayed, *Chem. Soc. Rev.* **2012**, *41*, 2740.
[22] S. Trigari, A. Rindi, G. Margheri, S. Sottini, G. Dellepiane, E. Giorgetti, *J. Mater. Chem.* **2011**, *21*, 6531.

[23] S. Barbosa, A. Agrawal, L. Rodríguez-Lorenzo, I. Pastoriza-Santos, R. A. Alvarez-Puebla, A. Kornowski, H. Weller, L. M. Liz-Marzán, *Langmuir* **2010**, *26*, 14943.
[24] D. Soukup, S. Moise, E. Céspedes, J. Dobson, N. D. Telling, *ACS Nano* **2015**, *9*, 231.
[25] S. Dutz, R. Hergt, *Int. J. Hyperthermia* **2013**, *29*, 790.
[26] a) P. Huang, J. Lin, W. Li, P. Rong, Z. Wang, S. Wang, X. Wang, X. Sun, M. Aronova, G. Niu, *Angew. Chem.* **2013**, *125*, 14208; b) J. Lin, S. Wang, P. Huang, Z. Wang, S. Chen, G. Niu, W. Li, J. He, D. Cui, G. Lu, *ACS Nano* **2013**, *7*, 5320.
[27] J. R. Navarro, D. Manchon, F. Lerouge, N. P. Blanchard, S. Marotte, Y. Leverrier, J. Marvel, F. Chaput, G. Micouin, A.-M. Gabudean, *Nanotechnology* **2012**, *23*, 465602.
[28] X. Wang, G. Li, Y. Ding, S. Sun, *RSC Adv.* **2014**, *4*, 30375.
[29] a) H. de Puig, J. O. Tam, C.-W. Yen, L. Gehrke, K. Hamad-Schifferli, *J. Phys. Chem. C* **2015**, *119*, 17408; b) G. Plascencia-Villa, D. Torrente, M. Marucho, M. José-Yacamán, *Langmuir* **2015**, *31*, 3527.
[30] H. Yuan, C. G. Khoury, H. Hwang, C. M. Wilson, G. A. Grant, T. Vo-Dinh, *Nanotechnology* **2012**, *23*, 075102.
[31] S. Freddi, L. Sironi, R. D'Antuono, D. Morone, A. Donà, E. Cabrini, L. D'Alfonso, M. Collini, P. Pallavicini, G. Baldi, D. Maggioni, G. Chirico, *Nano Lett.* **2013**, *13*, 2004.
[32] a) G. Plascencia-Villa, D. Bahena, A. R. Rodríguez, A. Ponce, M. José-Yacamán, *Metallomics* **2013**, *5*, 242; b) W. Jiang, B. Y. Kim, J. T. Rutka, W. C. Chan, *Nat. Nanotechnol.* **2008**, *3*, 145.
[33] H. Jo, H. Youn, S. Lee, C. Ban, *J. Mater. Chem. B* **2014**, *2*, 4862.
[34] L. Rodríguez-Lorenzo, Z. Krpetic, S. Barbosa, R. A. Alvarez-Puebla, L. M. Liz-Marzán, I. A. Prior, M. Brust, *Integr. Biol.* **2011**, *3*, 922.
[35] a) J. Conde, J. de la Fuente, P. Baptista, *Nanotechnology* **2010**, *21*, 505101; b) A. M. Schwartzberg, C. D. Grant, A. Wolcott, C. E. Talley, T. R. Huser, R. Bogomolni, J. Z. Zhang, *J. Phys. Chem. B* **2004**, *108*, 19191; c) Y. Yang, Y. Hu, H. Du, H. Wang, *Chem. Commun.* **2014**, *50*, 7287; d) A. L. Chen, Y. S. Hu, M. A. Jackson, A. Y. Lin, J. K. Young, R. J. Langsner, R. A. Drezek, *Nanoscale Res. Lett.* **2014**, *9*, 1.
[36] M. Aioub, B. Kang, M. A. Mackey, M. A. El-Sayed, *J. Phys. Chem. Lett.* **2014**, *5*, 2555.
[37] L. Rodríguez-Lorenzo, J. M. Romo-Herrera, J. Pérez-Juste, R. A. Alvarez-Puebla, L. M. Liz-Marzán, *J. Mater. Chem.* **2011**, *21*, 11544.
[38] C. Burda, X. Chen, R. Narayanan, M. A. El-Sayed, *Chem. Rev.* **2005**, *105*, 1025.
[39] J. D. Heidel, M. E. Davis, *Pharm. Res.* **2011**, *28*, 187.
[40] S. D. Perrault, C. Walkey, T. Jennings, H. C. Fischer, W. C. W. Chan, *Nano Lett.* **2009**, *9*, 1909.
[41] B. Enustun, J. Turkevich, *J. Am. Chem. Soc.* **1963**, *85*, 3317.
[42] N. G. Bastús, J. Comenge, V. Puntes, *Langmuir* **2011**, *27*, 11098.
[43] C. Graf, D. L. Vossen, A. Imhof, A. van Blaaderen, *Langmuir* **2003**, *19*, 6693.
[44] P. S. Kumar, I. Pastoriza-Santos, B. Rodriguez-Gonzalez, F. J. G. de Abajo, L. M. Liz-Marzan, *Nanotechnology* **2008**, *19*, 015606.